ADVANCED OPTICAL MATERIALS
www.advopticalmat.de

Quantification of Multiple Molecular Fingerprints by Dual-Resonant Perfect Absorber

*Arif E. Cetin, Semih Korkmaz, Habibe Durmaz, Ekin Aslan, Sabri Kaya, Roberto Paiella, and Mustafa Turkmen**

A dual-resonant perfect absorber (PA) based on multiple dipolar nanoantenna configuration is introduced. The PA platform exhibits near-unity (95%–98%) absorbance in dual-resonances. A fine-tuning mechanism of dual-resonances is determined via geometrical device parameters of the constituting dipolar elements of the compact PA system. It is also shown that the dual plasmonic resonances are associated with easily accessible and large local electromagnetic fields. Possessing large absorbance with strong nearfields, the PA system is highly advantageous for surface enhanced infrared absorption (SEIRA) spectroscopy applications. The simultaneous detection of absorption signals corresponding to C=O and C–H bands of a polymethyl methacrylate (PMMA) film, which are separated by as large as ≈1255 cm^{-1}, is experimentally shown. Furthermore, the interaction between plasmonic modes of the PA platform and the molecular vibrational modes of the PMMA film is investigated by tuning the optical resonances within the C=O spectral window. The coupling strength between plasmonic and vibrational modes is determined by Hamilton analysis, which leads to mode splitting and anticrossing behavior within the PA absorption spectra. The PA platform, by enabling simultaneous identification of different molecular fingerprints, can provide more reliable sensing information compared to classical SEIRA systems based only on a single vibrational mode.

1. Introduction

Perfect absorbers (PAs) are metamaterials, which can support near-unity absorbance within a narrow frequency range.[1–7] Their performance relies on an impedance matching, i.e., they support both electric and magnetic resonances, which are tuned to match their impedance ($Z = \sqrt{\mu/\varepsilon}$) to that of the surrounding medium. This match leads to a zero reflection coefficient so that the incident light is substantially absorbed. Landy et al. has shown the first PA, operating in microwave frequency range, where the structure consists of an electric resonator and a cut wire, which independently couple to electric and magnetic fields.[1] Later for the higher frequency ranges, Liu et al. demonstrated an infrared PA system.[8] The structure is composed of metal–dielectric–metal layers, where the top metal layer is patterned with subwavelength antennas serving as a resonator, and the bottom one is an optical mirror which significantly attenuates the transmittance. The coupling of light to the antennas induces an electric field, while the nearfield couplings between the antennas and the metal sheet result in mirror-image charges in the bottom layer. This generates a current loop which induces a magnetic field.[9–14] Then, tuning the amplitude and resonance frequency of the electric and magnetic responses can be used to match the impedance of PA to free-space, which minimizes the reflectance. Hence, minimizing reflection with impedance matching, while attenuating transmission with a metal sheet leads to perfect absorption. Recently, the dependence of absorbance on a critical coupling condition between resonators and optical mirrors has been investigated to provide a universal way for unity absorbance.[15] Supporting strong absorbance capabilities, PAs are good candidates for surface enhanced infrared absorption (SEIRA) spectroscopy applications. As the infrared region is accompanied with low radiation damping, PAs engineered at this wavelength window could support plasmonic resonances with high Q-factors, which leads to strong nearfield enhancements. This feature is highly advantageous for achieving large spectroscopic signals associated with the molecular vibrational modes of interest.[16–22] In order to reliably identify the targeted molecules, it is crucial to simultaneously monitor different molecular fingerprints. However, PAs' unity absorbance is limited within a narrow spectral window where the plasmonic resonances of their subwavelength antennas lie. This problem could be addressed by utilizing nanoparticle or nanoaperture based configurations, supporting multiple resonances.[23–31] Recently, different multiband PA structures have been introduced to serve for variety of applications from microwave to mid-infrared frequency ranges.[32–39]

Dr. A. E. Cetin
Koch Institute for Integrative Cancer Research
Massachusetts Institute of Technology
Cambridge, MA 02139, USA
S. Korkmaz, E. Aslan, Dr. S. Kaya, Dr. M. Turkmen
Department of Electrical and Electronics Engineering
Erciyes University
38039 Kayseri, Turkey
E-mail: turkmen@erciyes.edu.tr
Dr. H. Durmaz, Dr. R. Paiella
Department of Electrical and Computer Engineering
Boston University
MA 02215, USA

DOI: 10.1002/adom.201600305

Here, we introduce a PA platform supporting near-unity absorbance in dual-resonances within the mid-infrared frequency range for simultaneous detection of multiple molecular fingerprints in SEIRA applications. The proposed sensing platform is composed of multiple gold (Au) nanorod antennas on a thin magnesium fluoride (MgF_2) interlayer separating them from an optically thick gold sheet. The dual-resonant behavior arises due to the multiple dipolar modes of the constituting antenna elements in the compact PA system. The PA platform supports near-unity absorption (between 95% and 98%) in dual-resonances. More importantly, the PA system maintains the amplitude and linewidth of the resonances while spectrally tuning the plasmonic modes by geometrical device parameters. The dual-resonances are also associated with large local electromagnetic fields, which are highly sensitive to variations within the surrounding medium. Hence, supporting multiple near-unity absorbance with accessible and large nearfields, our dual-resonant PA platform is highly advantageous for SEIRA applications. We demonstrate the SEIRA capability of our PA system by simultaneously monitoring C=O and C—H bands of a 10 nm-thick polymethyl methacrylate (PMMA) film. Finally, tuning the PA resonances within the spectral window of the molecular bands, we investigate the strength of the interaction between plasmonic modes of the PA platform and the vibrational modes of the PMMA film, which leads to anticrossing and splitting of resonances.

2. Results and Discussion

Schematics and scanning electron microscope (SEM) image of the dual-resonant PA platform are shown in **Figure 1**A,B, respectively. The unit cell of a PA (denoted with a white square

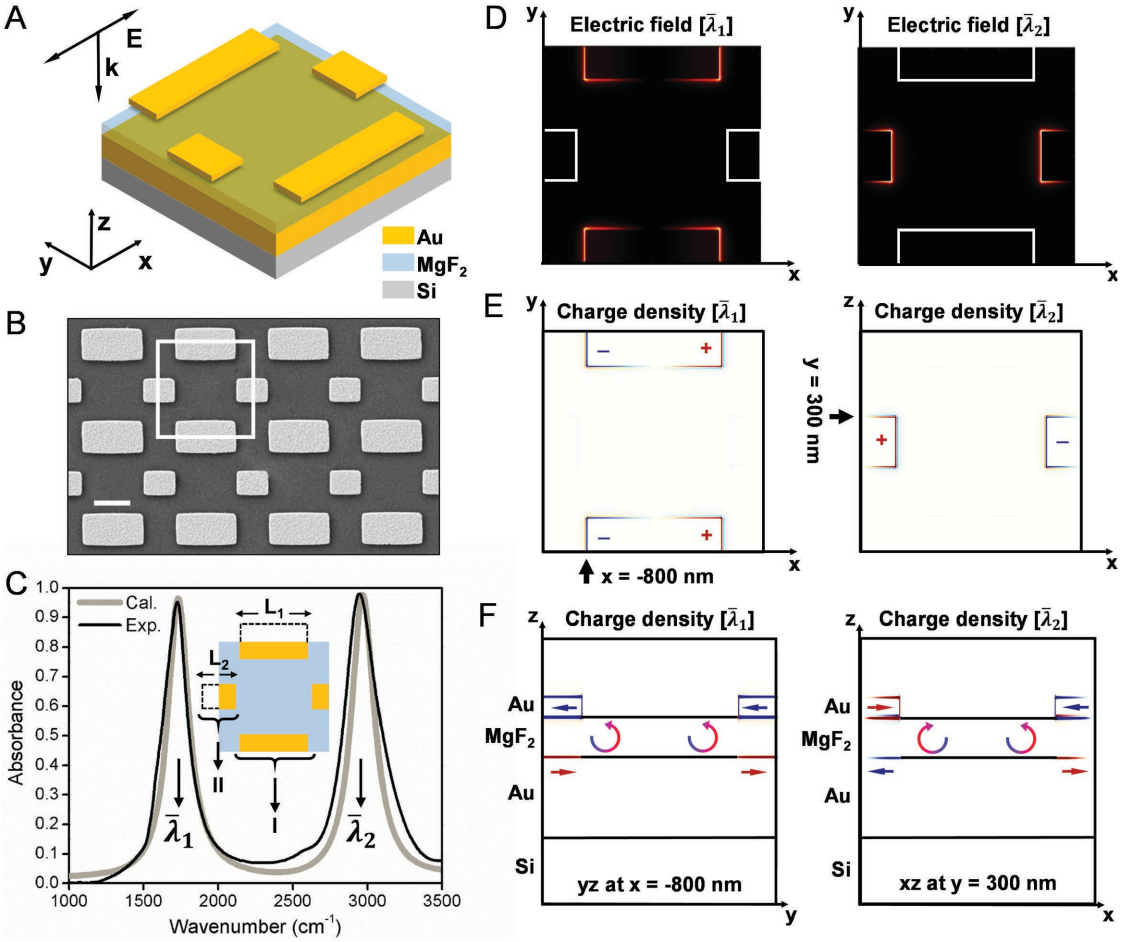

Figure 1. A) Schematics and B) SEM image of the PA design, composed of Au nanorod antennas on an Au sheet separated by an MgF_2 interlayer. In (A), propagation and polarization directions of the illumination source are illustrated. The white square in (B) is the PA unit cell. Scale bar, 2 μm. C) Calculated (grey) and experimental (black) absorbance spectra of the PA platform. Figure inset illustrates the device dimensions. Modes located at $\bar{\lambda}_1$ and $\bar{\lambda}_2$ are associated with nanorod antenna-I and antenna-II with lengths L_1 and L_2, respectively. D) Electric field intensity enhancement and E) charge distributions (exhibiting a dipolar electric resonance) calculated at the top surface of the antennas at $\bar{\lambda}_1$ and $\bar{\lambda}_2$. F) Cross-sectional profile of the charge distributions, demonstrating the mirror-image charges at the antennas and the Au sheet inducing the antiparallel currents denoted by the arrows (generating a dipolar magnetic resonance). Charge distributions for the mode at $\bar{\lambda}_1$ is calculated through *yz* cross-section at $x = -800$ nm and the one for the mode at $\bar{\lambda}_2$ is calculated through *xz* cross-section at $y = 300$ nm, denoted with arrows in (E). The corresponding device parameters: $L_1 = 1600$ nm, $L_2 = 800$ nm, widths of the antenna-I and antenna-II are 800 and 600 nm, respectively, and array periodicity is 2.6 μm. The PA platform is composed of 50 nm-thick Au rod antennas, 100 nm-thick MgF_2 interlayer, and 200 nm-thick Au film.

DOI: 10.1002/adom.201600305

in Figure 1B) consists of four Au nanorods and an optically thick Au sheet, which are separated by an MgF_2 interlayer. The whole system is fabricated on a silicon (Si) substrate. Polarization of the illumination source (illustrated in Figure 1A) is along the longer sides of the antennas. Figure 1C shows the calculated (grey) and experimental (black) absorbance spectra of the PA platform, coinciding well with one another both in magnitude and spectral position. Here, absorption is defined as $A = 1 - R - T$. PA system supports two absorption peaks obtained experimentally at $\bar{\lambda}_1 = 1727\ \mathrm{cm}^{-1}$ and $\bar{\lambda}_2 = 2948\ \mathrm{cm}^{-1}$ with 95% and 98% absorbance, respectively. The overall PA is composed of dipolar antennas of two different rod lengths, e.g., antenna-I with L_1 and antenna-II with L_2 (illustrated in Figure 1C-inset). Between different PA cell options, due to the symmetric nature of the overall antenna system along *x*- and *y*-directions, the unit cell is chosen in a way that it includes halves of antenna-I and antenna-II. Resonant wavelength of the first order dipolar plasmonic excitations for a nanorod antenna with length L occurs approximately at $\lambda_{res} = 2Ln_{eff} + C$, where n_{eff} is the effective refractive index of the surrounding medium composed of the supporting substrate under the antennas and the medium in the vicinity (i.e., air or a cladding medium).[16,40] The double absorbance peaks arise as a superposition of the plasmonic excitations of the two rod nanoantennas with different lengths, where the modes observed at longer wavelengths (smaller wavenumbers, $\bar{\lambda}_1$) is associated with the longer antenna (L_1) while the one at shorter wavelengths (larger wavenumbers, $\bar{\lambda}_2$) is associated with the shorter antenna (L_2). Figure 1D shows the nearfield intensity enhancement distributions ($|E|^2/|E_{incident}|^2$) calculated at two resonances via finite difference time domain (FDTD) simulations, where large local electromagnetic fields are concentrated at the tip ends of the corresponding dipolar antennas along the polarization direction, demonstrating their dipolar nature. Incident light radiation polarizes the antennas at opposite ends as shown by the charge distribution calculated at the top surface of the antennas (Figure 1E). As the antennas and Au sheet are separated with a thin MgF_2 interlayer, nearfield couplings between them are strong, i.e., the induced image charges at the Au sheet result in antiparallel currents (illustrated with arrows along the direction of the current flow in Figure 1F), which create a magnetic dipole. These generated electric and magnetic dipoles by polarization and current loop, can enable to tune the effective permittivity and permeability of the PA platform.[32] Impedance matching to free-space by tuning permittivity and permeability minimizes the reflection, while transmission is attenuated by the Au sheet such that a near-unity absorbance is achieved at two well-separated spectral positions as shown in Figure 1C.

As the dual-resonances originate from the superposition of the two individual dipolar modes of antennas with different lengths (L_1 and L_2), their spectral positions can be independently tuned by the rod lengths.[16] In order to experimentally demonstrate this phenomenon, we manufacture PA structures with e-beam lithography based fabrication scheme as described in the Experimental Section. In this article, we particularly focus on the spectral variations within the mode at longer wavelengths ($\bar{\lambda}_1$) for SEIRA applications. **Figure 2**A shows the

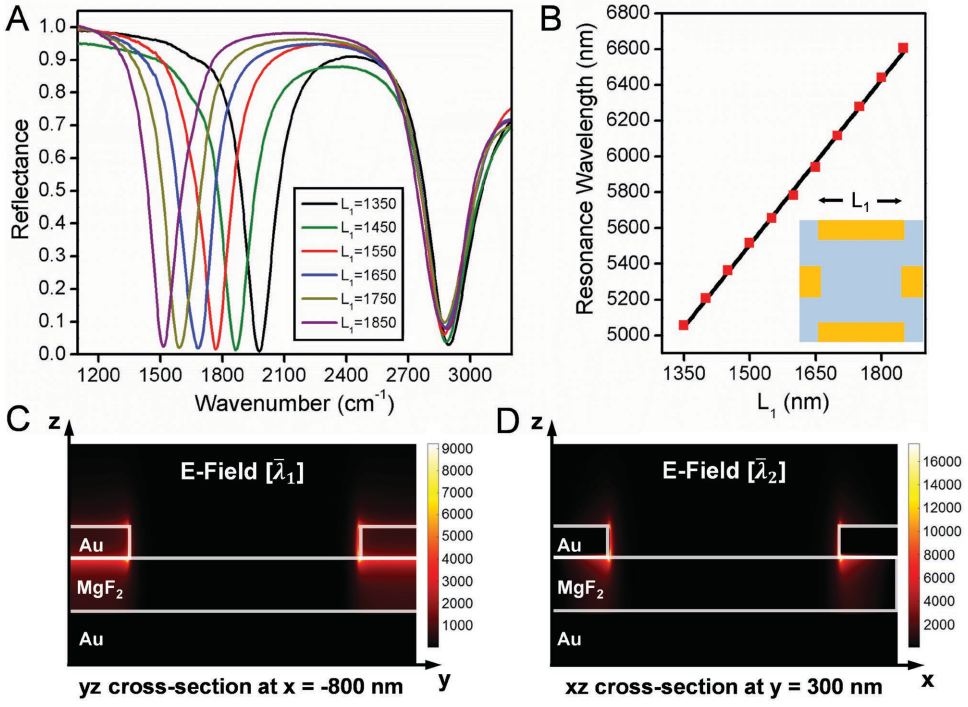

Figure 2. A) Experimental reflection spectra of the PA platform for different L_1 lengths, while L_2 is kept constant, which shifts the mode at $\bar{\lambda}_1$ whereas the mode at $\bar{\lambda}_2$ shows negligible variations. B) Resonance wavelength of the mode at $\bar{\lambda}_1$ versus rod length L_1, demonstrating their linear relationship. The figure inset illustrates the longer dipolar antenna in the compact PA platform. Electric field intensity enhancement distributions for the modes at C) $\bar{\lambda}_1$ (*yz* cross-section at $x = -800$ nm) and D) $\bar{\lambda}_2$ (*xz* cross-section at $y = 300$ nm), respectively. The corresponding device parameters for L_1 variation: $L_2 =$ 800 nm, widths of the antenna-I and antenna-II are 800 and 600 nm, respectively, and array periodicity is 2.6 μm. The PA platform is composed of 50 nm-thick Au rod antennas, 100 nm-thick MgF_2 interlayer, and 200 nm-thick Au sheet. Cross-sectional nearfield calculations are shown for $L_1 = 1600$ nm.

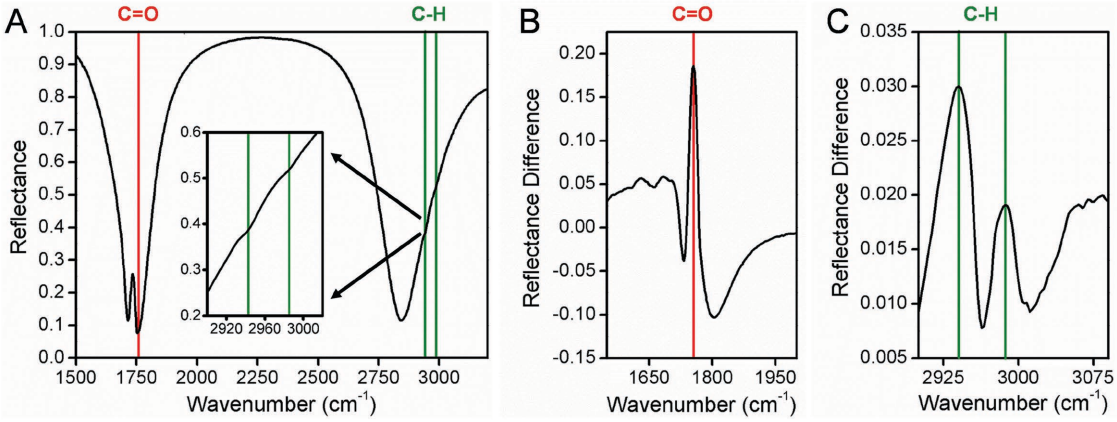

Figure 3. A) Reflectance spectrum of the PA system coated with a 10 nm-thick PMMA film. Figure inset shows the zoom image of the C—H band. Reflection difference spectra of B) C=O and C) C—H bands. Red and green lines denote the spectral positions of C=O and C—H bands, respectively. The corresponding device parameters: L_1 = 1550 nm, L_2 = 800 nm, widths of the antenna-I and antenna-II are 800 and 600 nm, respectively, and array periodicity is 2.6 μm. The PA platform is composed of 50 nm-thick Au rod antennas, 100 nm-thick MgF_2 interlayer, and 200 nm-thick Au sheet.

reflectance spectra for different L_1 lengths, where the mode at $\bar{\lambda}_1$ shifts to longer wavelengths (smaller wavenumbers) for larger L_1. The spectral measurement is performed through Fourier transform infrared (FTIR) spectroscopy as explained in the Experimental Section. Figure 2B shows the resonance wavelength of the mode at $\bar{\lambda}_1$ for different rod lengths L_1 while L_2 is kept constant, demonstrating the expected linear relationship between the resonance wavelength and rod length as discussed earlier. On the other hand, the mode associated with L_2 does not show any spectral variation with L_1. More importantly, the two resonances at $\bar{\lambda}_1$ and $\bar{\lambda}_2$ have similar absorbance even though they are separated by more than 1200 cm^{-1}. Another important feature of our PA platform is that linewidth and amplitude of the dual-resonances show negligible variations for different rod lengths, as there is no coupling between constituting dipolar antennas. These properties are highly advantageous for SEIRA applications on simultaneous identification of different molecular fingerprints. Supporting Information shows L_1 and L_2 variations, demonstrating the independent fine-tuning of dual-resonances with rod lengths. For SEIRA applications, it is also critical to excite plasmonic modes with large nearfield enhancements. Figure 2C,D shows the calculated cross-sectional profiles of the nearfield intensity enhancement for the modes at $\bar{\lambda}_1$ and $\bar{\lambda}_2$, respectively. Here, large quantity of the local electromagnetic fields are concentrated at the surface of the antennas and extend extensively within the surrounding medium, which makes them highly accessible for targeted biochemical molecules in the vicinity of the PA platform. Hence, generating large nearfields at well-separated two spectral locations can enable the simultaneous identification of different molecular fingerprints through the interaction between molecular vibrational modes and local electromagnetic fields associated with different plasmonic excitations. This phenomenon is very important to provide more reliable sensing information on targeted molecules compared to the one relying on only a single vibrational mode.

In order to maximize the spectroscopy signals, it is critical to tune the resonance frequencies to the vibrational modes of interest.[40] Supporting dual-resonances with unity absorbance and easily accessible large local fields, our PA platform is a good candidate for SEIRA applications. Consequently, we perform simultaneous detection of two vibrational modes of a 10 nm-thick PMMA film. The PMMA thickness is determined through ellipsometry measurements (Woollam).[16,40] We design our system to detect C—H and C=O bands of the PMMA. **Figure 3**A shows the reflection spectra of the PA platform coated with the PMMA film. The molecular signatures are observed as reflectance dips (absorption peaks), where the one observed at 1755 cm^{-1} corresponds to C=O band stretch (red line) and the two dips at 2945 cm^{-1} and 2985 cm^{-1} correspond to C—H band stretch (green lines). PMMA has a complex permittivity, where the imaginary (dispersive) part accounts for the absorption (reflection dips). On the other hand, the real (nondispersive) part increases the effective refractive index of the surrounding medium such that the plasmonic resonances also shift to longer wavelengths (smaller wavenumbers by ≈20 cm^{-1}, not shown here). Figure 3B,C shows the reflection difference spectra for C—H and C=O absorption bands, respectively. In order to reliably calculate the reflection difference ($\Delta R = R_{fit} - R_{PMMA}$) in the presence of the spectral shifts, we employ a polynomial fitting procedure which shifts the bare response and performs a baseline fitting such that the PA reflectance before PMMA coating (R_{fit}) fairly overlaps with the one after PMMA coating (R_{PMMA}). As shown in Figure 3B,C, C=O stretch intensity is larger than that of C—H due to its larger dipole moment. Here, the better spectral overlap between plasmonic resonance and C=O band further increases the reflectance difference compared to C—H band. Our results also indicate that we can even detect vibrational signatures corresponding to bands with weak dipole moments, i.e., C—H band. These features are very advantageous to demonstrate simultaneous detection of multiple fingerprints of biochemical molecules.

As shown in Figure 3B, the symmetric Lorentzian shape of C=O vibrational mode no more exists (Lorentzian shape of the mode can be seen from the imaginary part of the PMMA refractive index in Figure 5B), instead it shows a Fano-like profile. Furthermore, the reflection dip corresponding to C=O band (1755 cm^{-1}, denoted with a red line in Figure 3A) shifts

Adv. Optical Mater. **2016**,
DOI: 10.1002/adom.201600305

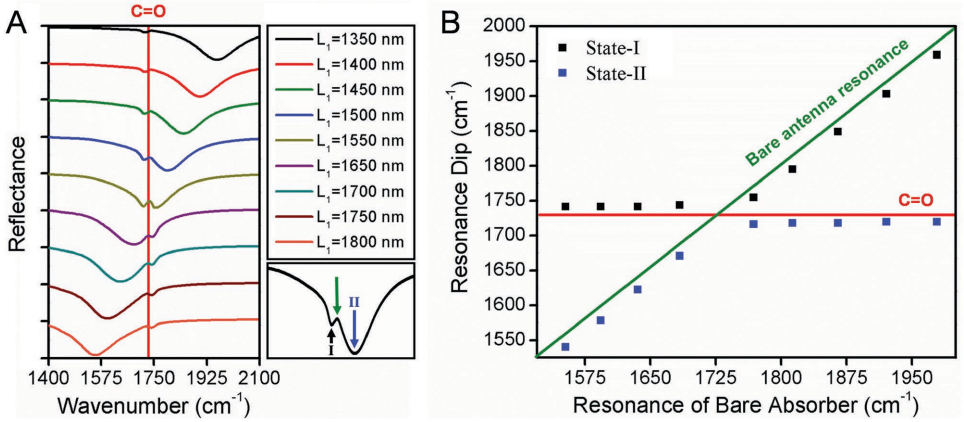

Figure 4. A) Reflectance spectrum of the PA coated with a 10 nm-thick PMMA film for different L_1 lengths. The red line denotes the spectral position of C=O band. Figure inset shows the hybridized modes (I = black arrow, II = blue arrow) and the reflection peak (green arrow) within the PA resonance. B) The spectral position of the hybridized modes (I = black dots, II = blue dots) with respect to the resonance wavelength of the PA before PMMA coating. Redline denotes the C=O vibrational band. Green line, Slope = 1. The corresponding device parameters for L_1 variation: L_2 = 800 nm, widths of the antenna-I and antenna-II are 800 and 600 nm, respectively, and array periodicity is 2.6 μm. The PA platform is composed of 50 nm-thick Au rod antennas, 100 nm-thick MgF_2 interlayer, and 200 nm-thick Au sheet.

from the original position of this band (1731 cm^{-1}). These spectral variations are due to the strong interaction between the plasmonic modes of PA and the PMMA vibrational modes.[9,32,41] In **Figure 4**A, we investigate the effect of this interaction by monitoring the spectral variations after PMMA coating the antennas with optical responses as shown in Figure 2A (C=O band at 1731 cm^{-1} is highlighted with a red line in Figure 4A). For the antennas supporting a plasmonic resonance at >1731 cm^{-1} (L_1 = 1350, 1400, 1450, 1500 nm), the reflection dip corresponding to C=O band is observed at smaller wavenumbers, while for the one supporting resonances at <1731 cm^{-1} (L_1 = 1650, 1700, 1750, 1800 nm), it is observed at larger wavenumbers. When the plasmonic and vibrational modes are closely matched, a clear splitting is observed (L_1 = 1550). Figure 4B shows the spectral position of the two reflection dips (denoted with black and blue arrows in Figure 4A-inset) with respect to the resonance wavelength of the PAs before PMMA coating. Here, the splitting of optical modes resulting in two reflectance dips (denoted with I and II in Figure 4A-inset) is due to the hybridization between the plasmonic mode of the PA and C=O vibrational mode. As these two hybridized states coherently interfere which reduces absorption, we observe a peak within the plasmonic resonance (highlighted with a green arrow in Figure 4A-inset). In Figure 4B, the red line denotes the resonance wavenumber of C=O band (1731 cm^{-1}) and the green line denotes the bare resonance of the PA (slope = 1) for the mode corresponding to the dipolar antenna-I with length, L_1. For the PA systems supporting plasmonic resonances detuned from the C=O band, the energy states lie at their initial positions. The discrepancy between the bare resonances (green line) and the spectral dips is due to the real part of the PMMA permittivity, shifting the plasmonic modes to longer wavelengths. As the plasmonic resonances are tuned to C=O band, the interaction between plasmonic and vibrational modes becomes stronger such that we observe an asymmetric mode splitting and anticrossing. Similar effects have been previously reported in association with plasmon-molecule coupling in subwavelength antenna configurations.[22,42]

In order to estimate the coupling strength between plasmonic and vibrational modes, we model the PA system covered with a 10 nm-thick PMMA film through FDTD simulations. The permittivity of the PMMA layer is obtained by infrared reflection absorption spectroscopy. In simulations, we use a Lorentz model for the PMMA permittivity where we fit an oscillator to the experimental data: $\varepsilon_{\text{bilayer}} = \varepsilon_\infty + (S/(\omega_p^2 - \omega^2 - i\omega\gamma_p)$, where ε_∞ = 2.36 is the high frequency constant term, ω_p = 3.26 × 10^{14} (rad s^{-1}) is the oscillator resonance frequency, γ_p = 3.72 × 10^{12} (rad s^{-1}) is the damping frequency and S = 1.22 × 10^{27} (rad s^{-1})^2 is the oscillator strength. **Figure 5**A,B shows the real and imaginary parts of the PMMA permittivity. Figure 5C shows the reflection spectra of the PA platform covered with PMMA, where the C=O band stretch can be seen as a reflection dip at 1765 cm^{-1} (denoted with a red line). Figure 5D shows the spectral position of the two hybridized states (denoted with I = black and II = blue) with respect to the PA resonance wavelength before PMMA coating. In the figure, the red line denotes the resonance wavenumber of C=O band (1731 cm^{-1}) and the green line denotes the bare resonance of the PA (slope = 1). Here, the Hamiltonian of the PA–PMMA system can be written as $H = \begin{bmatrix} E_{PA} & V \\ V & E_{C=O} \end{bmatrix}$, where E_{PA} is the independent energy of the PA resonance after the redshift due to the real part of the PMMA permittivity, and $E_{C=O}$ is the energy of C=O vibrational mode. The Hamiltonian has the eigenvalues $E_{I,II} = (E_{PA} + E_{C=O})/2 \pm \sqrt{(E_{PA} - E_{C=O})^2/4 + V^2}$, where rearranging the terms yields the coupling energy: $V = 0.5\sqrt{(E_I - E_{II})^2 - (E_{PA} - E_{C=O})^2}$. Inserting E_I, E_{II}, E_{PA} (E_{PA} is determined from the PA system covered with a dielectric layer possessing only the real part of the PMMA permittivity) and $E_{C=O}$, we calculate the coupling energy as 2.8 eV. This value is much larger than typical molecular vibration transitions, demonstrating that our PA platform successfully enhances light–matter interaction. Furthermore our PA platform, supporting

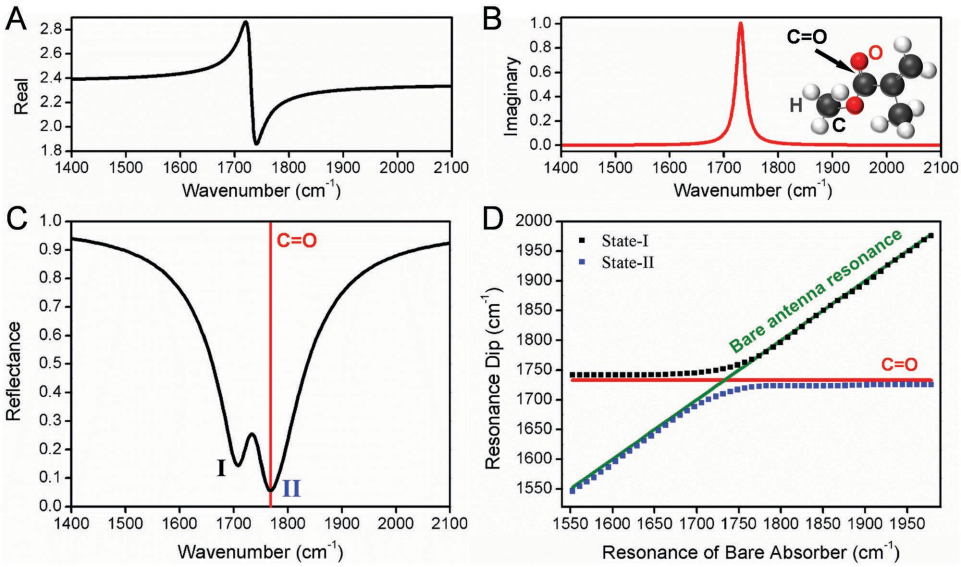

Figure 5. A) Real and B) imaginary parts of the PMMA permittivity. Inset of (B) shows the schematic illustration of PMMA vibrational modes. C) Calculated reflectance spectrum of the PA coated with a 10 nm-thick PMMA film for L_1 = 1550 nm. In the figure, I = black arrow and II = blue arrow denote the hybridized states. The red line denotes the spectral position of C=O band. D) The spectral position of the hybridized modes (I = black dots, II = blue dots) with respect to the resonance wavelength of the PA before PMMA coating. Red line denotes the C=O vibrational band. Green line, Slope = 1. The corresponding device parameters for L_1 variation: L_2 = 800 nm, widths of the antenna-I and antenna-II are 800 and 600 nm, respectively, and array periodicity is 2.6 μm. The PA platform is composed of 50 nm-thick Au rod antennas, 100 nm-thick MgF_2 interlayer, and 200 nm-thick Au sheet.

high Q-factor plasmonic resonances with highly accessible large local electromagnetic fields at multiple spectral positions, enables simultaneous identification of different molecular fingerprints providing more reliable sensing information compared to classical SEIRA systems based on only a single vibrational mode.

3. Conclusions

We introduce a dual-resonant PA system, utilizing multiple dipolar antennas in a compact platform. We show that our PA platform supports dual high Q-factor plasmonic resonances with near-unity absorbance as well as large and easily accessible local electrometric fields. We demonstrate our PA platform's highly advantageous character in SEIRA applications through simultaneous monitoring of widely separated C=O and C—H bands of a thin PMMA film. In addition to absorption signatures within the PA reflection spectra observed as spectral dips, we also showed variations within the shape and position of the plasmonic resonances, which are directly associated with the strong interaction between PA plasmonic modes and PMMA vibrational modes. We investigate this interaction via the Hamilton eigenvalue analysis to show our platform's strong light–mater interaction capability. Our platform, supporting highly advantageous far- and nearfield characteristics, can enable simultaneous detection of different molecular fingerprints of targeted biochemical molecules, which could provide more reliable information compared to classical SEIRA systems relying only on a single vibrational information.

4. Experimental Section

PA Fabrication: Au sheet and MgF_2 interlayer were deposited on a silicon wafer with CHA e-beam evaporator. E-beam lithography (Zeiss-Supra 40 VP) was performed on a PMMA film (Michrochem 950-A5) covering the MgF_2 interlayer. After development, Au was deposited, followed by a lift-off process with acetone, which results in the PA platform.

FTIR Measurements: Reflection data were collected by a Fourier transform infrared spectrometer (Bruker, VERTEX 70V) coupled to an infrared microscope (Bruker, Hyperion 1000). The spectra were collected with 4 cm^{-1} resolution, consisting of 256 scans coadded with a mirror repetition rate of 20 kHz. All measurements were performed under a dry-air purged condition to eliminate atmospheric water vapor absorption.

Supporting Information

Supporting Information is available from the Wiley Online Library or from the author.

Acknowledgements

A.E.C., S.K., and H.D. contributed equally to this work. Turkmen Research Group acknowledges The Scientific and Technological Research Council of Turkey (TUBITAK) under the Project No: 113E277.

Received: April 24, 2016
Published online:

[1] N. I. Landy, S. Sajuyigbe, J. J. Mock, D. R. Smith, W. J. Padilla, *Phys. Rev. Lett.* **2008**, *100*, 207402.
[2] K. Aydin, V. E. Ferry, R. M. Briggs, H. A. Atwater, *Nat. Commun.* **2011**, *2*, 517.
[3] Z. Li, S. Butun, K. Aydin, *ACS Nano* **2014**, *8*, 8242.

[4] N. Liu, M. Mesch, T. Weiss, M. Hentschel, H. Giessen, *Nano Lett.* **2010**, *10*, 2342.
[5] J. A. Mason, G. Allen, V. A. Podolskiy, D. Wasserman, *IEEE Photonics Technol. Lett.* **2012**, *24*, 31.
[6] L. V. Brown, X. Yang, K. Zhao, B. Y. Zheng, P. Nordlander, N. J. Halas, *Nano Lett.* **2015**, *15*, 1272.
[7] G. M. Akselrod, J. Huang, T. B. Hoang, P. T. Bowen, L. Su, D. R. Smith, M. H. Mikkelsen, *Adv. Mater.* **2015**, *27*, 8034.
[8] X. Liu, T. Starr, A. F. Starr, W. J. Padilla, *Phys. Rev. Lett.* **2010**, *104*, 207403.
[9] Y. Li, L. Su, C. Shou, C. Yu, J. Deng, Y. Fang, *Sci. Rep.* **2013**, *3*, 2865.
[10] J. Hendrickson, B. Zhang, J. Guo, *J. Opt. Soc. Am. B* **2013**, *30*, 656.
[11] Y. Cui, K. H. Fung, J. Xu, S. He, N. X. Fang, *Opt. Express* **2012**, *20*, 17552.
[12] Y. L. Liao, Y. Zhao, *Optik* **2014**, *125*, 3037.
[13] Z. H. Jiang, S. Yun, F. Toor, D. H. Werner, T. S. Mayer, *ACS Nano* **2011**, *5*, 4641.
[14] K. Chen, T. D. Dao, S. Ishii, M. Aono, T. Nagao, *Adv. Funct. Mater.* **2015**, *25*, 6637.
[15] R. Adato, A. Artar, S. Erramilli, H. Altug, *Nano Lett.* **2013**, *13*, 2584.
[16] R. Adato, A. A. Yanik, J. J. Amsden, D. L. Kaplan, F. G. Omenetto, M. K. Hong, S. Erramilli, H. Altug, *Proc. Natl. Acad. Sci. USA* **2009**, *106*, 19227.
[17] K. Ataka, J. Heberle, *Anal. Bioanal. Chem.* **2007**, *388*, 47.
[18] J. Kundu, F. Le, P. Nordlander, N. J. Halas, *Chem. Phys. Lett.* **2008**, *452*, 115.
[19] T. H. Taminiau, F. D. Stefani, F. B. Segerink, N. F. Van Hulst, *Nat. Photonics* **2008**, *2*, 234.
[20] C. Wu, A. B. Khanikaev, R. Adato, N. Arju, A. A. Yanik, H. Altug, G. Shvets, *Nat. Mater.* **2012**, *11*, 69.
[21] R. Adato, H. Altug, *Nat. Commun.* **2013**, *4*, 2154.
[22] F. Neubrech, A. Pucci, T. W. Cornelius, S. Karim, S. A. Garcia-Extarri, J. Aizpurua, *Phys. Rev. Lett.* **2008**, *101*, 157403.
[23] J. Shu, W. Gao, K. Reichel, D. Nickel, J. Dominguez, I. Brener, D. M. Mittleman, Q. Xu, *Opt. Express* **2014**, *22*, 3747.
[24] A. E. Cetin, M. Turkmen, S. Aksu, H. Altug, *IEEE Trans. Nanotechnol.* **2012**, *11*, 208.
[25] G. Kumar, A. Cui, S. Pandey, A. Nahata, *Opt. Express* **2011**, *19*, 1072.
[26] A. E. Serebryannikov, M. Beruete, M. Mutlu, E. Ozbay, *Opt. Express* **2015**, *23*, 13517.
[27] A. E. Cetin, S. Kaya, A. Mertiri, E. Aslan, S. Erramilli, H. Altug, M. Turkmen, *Photonics Nanostruct.* **2015**, *15*, 73.
[28] L. Wu, Z. Yang, M. Zhao, Y. Zheng, J. A. Duan, X. Yuan, *Opt. Express* **2014**, *22*, 14588.
[29] M. Turkmen, A. E. Cetin, S. Aksu, A. A. Yanik, H. Altug, *Opt. Express* **2011**, *19*, 7921.
[30] M. Jahn, S. Patze, I. J. Hidi, R. Knipper, A. I. Radu, A. Mühlig, S. Yüksel, V. Peksa, K. Weber, T. Mayerhöfer, D. Cialla-May, *Analyst* **2016**, *141*, 756.
[31] A. E. Cetin, M. Turkmen, S. Aksu, D. Etezadi, H. Altug, *Appl. Phys. B* **2015**, *118*, 29.
[32] K. Chen, R. Adato, H. Altug, *ACS Nano* **2012**, *6*, 7998.
[33] Y. Zhang, T. Li, Q. Chen, H. Zhang, J. F. O'Hara, E. Abele, A. J. Taylor, H. T. Chen, A. K. Azad, *Sci. Rep.* **2015**, *5*, 18463.
[34] B. X. Wang, X. Zhai, G. Z. Wang, W. Q. Huang, L. L. Wang, *J. Appl. Phys.* **2015**, *117*, 014504.
[35] S. Li, J. Gao, X. Cao, Z. Zhang, Y. Zheng, C. Zhang, *Opt. Express* **2015**, *23*, 3523.
[36] H. R. Seren, G. R. Keiser, L. Cao, J. Zhang, A. C. Strikwerda, K. Fan, G. D. Metcalfe, M. Wraback, X. Zhang, R. D. Averitt, *Adv. Opt. Mater.* **2014**, *2*, 1221.
[37] Y. J. Yoo, Y. J. Kim, P. V. Tuong, J. Y. Rhee, K. W. Kim, W. H. Jang, Y. H. Kim, H. Cheong, Y. P. Lee, *Opt. Express* **2013**, *21*, 32484.
[38] L. Li-Yang, W. Jun, D. Hong-Liang, W. Jia-Fu, Q. Shao-Bo, *Chin. Phys. B* **2015**, *24*, 064201.
[39] H. B. Baskey, M. J. Akhtar, A. K. Dixit, T. C. Shami, *J. Electromagn. Waves Appl.* **2015**, *29*, 2479.
[40] R. Adato, A. A. Yanik, C. H. Wu, G. Shvets, H. Altug, *Opt. Express* **2010**, *18*, 4526.
[41] G. A. Wurtz, P. R. Evans, W. Hendren, R. Atkinson, W. Dickson, R. J. Pollard, A. V. Zayats, W. Harrison, C. Bower, *Nano Lett.* **2007**, *7*, 1297.
[42] V. Giannini, Y. Francescato, H. Amrania, C. C. Phillips, S. A. Maier, *Nano Lett.* **2011**, *11*, 2835.